Polymer Chemistry

ROYAL SOCIETY OF CHEMISTRY

PAPER

View Article Online
View Journal | View Issue

Cite this: *Polym. Chem.*, 2026, **17**, 2167

Design and application of nanosilver hybridized fluorosilicone resin-modified epoxy coatings for SRB resistance in aviation fuel storage and transport equipment

Lanjiao Jiao, Xiaojuan Lai and Qiufeng An *

Microbiologically influenced corrosion poses a significant threat to the service life and safety of metallic aviation fuel infrastructure. To address this challenge, this study reports the rational design and fabrication of a multifunctional epoxy composite coating (SNA-FPS/ER) with integrated hydrophobic, antimicrobial, and anticorrosive properties. The coating was engineered through a synergistic strategy: first, aminosilane-encapsulated silver nanoparticles (SNA) were synthesized *via* a sol–gel process to ensure dispersion stability and provide a sustained-release bactericidal function; second, a tailored amino-fluorosilicone resin (FPS) was prepared by hydrolytic co-condensation to act as a curing agent and modifier, simultaneously toughening the epoxy network and imparting surface hydrophobicity. Systematic evaluation revealed that the SNA-FPS/ER coatings containing 0.5–2.0 wt% SNA exhibited excellent mechanical properties, including grade 1 adhesion and 5H pencil hardness, and resisted blistering or wrinkling after 1000 h of jet fuel immersion. Electrochemical measurements indicated an optimal corrosion protection performance at 1 wt% SNA loading, with a low-frequency impedance of 5×10^4 Ω cm^2 and a corrosion current density of 7.35×10^{-8} A cm^{-2}. The coatings demonstrated potent, dose-dependent antimicrobial activity, achieving bactericidal rates >99% against *E. coli* and *S. aureus*. Furthermore, after 7-day immersion in a sulfate-reducing bacteria (SRB) suspension (10^4 CFU mL^{-1}), coatings with 2 wt% SNA remained visually intact, confirming exceptional resistance to microbially induced corrosion. This work presents a viable material solution, achieved through deliberate polymer and nanocomposite design, for protecting aviation fuel systems against complex degradation pathways.

Received 2nd December 2025,
Accepted 4th May 2026

DOI: 10.1039/d5py01145k

rsc.li/polymers

1. Introduction

Microbiologically-influenced corrosion (MIC) represents a formidable industrial challenge, manifesting ubiquitously across offshore platforms, aerospace systems, and built environments.[1] It incurs substantial economic penalties and poses significant safety hazards.[2] In the United States oil and gas sector alone, MIC is estimated to account for approximately 20% of total corrosion-related losses, amounting to $100 million annually.[3] Within aviation fuel systems, over 200 species of microorganisms have been identified; their metabolic proliferation generates slime, sludge, and acidic by-products including organic acids, hydrogen sulfide, and sulfuric acid which not only obstruct filtration apparatuses and distort fuel gauge readings but also induce severe corrosion of storage tanks and pipelines.[4,5] Such degradation can precipitate fuel leakage and, in extreme scenarios, catastrophic fire or explosion. Among the implicated microbiota, sulfate-reducing bacteria (SRB) are principal culprits in the generation of reservoir H_2S and the accelerated deterioration of metallic infrastructure.[6–8] As anaerobic, corrosive microorganisms, SRB enzymatically reduce sulfate to sulfide ions (S^{2-}) during respiration, which subsequently react with metal ions to form metallic sulfides, thereby directly catalyzing the corrosion process.[9] Given that aviation fuel storage and transport hardware is predominantly metallic, SRB readily colonize these surfaces, forming tenacious biofilms that exacerbate material degradation. Consequently, the mitigation of SRB-induced corrosion is paramount to ensuring the operational safety and extended service life of fuel containment and delivery systems.[10]

Current strategies for addressing MIC encompass physical remediation (*e.g.*, mechanical cleaning) and chemical intervention (*e.g.*, biocide application).[11] Conventional protective regimes integrate corrosion inhibitors, antimicrobial agents, and barrier coatings.[12–14] While corrosion inhibitors effectively

Shaanxi Key Laboratory of Chemical Additives for Industry, College of Chemistry and Chemical Engineering, Shaanxi University of Science and Technology, Xi'an, 710021, China. E-mail: aqf@sust.edu.cn

attenuate galvanic corrosion rates and antimicrobials suppress planktonic or sessile SRB populations, these standalone measures seldom afford durable, long-term protection.[15,16] Accordingly, polymeric barrier coatings have emerged as the preeminent solution for metal preservation, with epoxy, acrylic, polyurethane, and alkyd resins being the most widely deployed systems.[17,18] Epoxy coatings, in particular, are valued for their robust mechanical integrity, chemical inertness, and exceptional substrate adhesion, establishing them as cornerstones of corrosion mitigation.[19–21] Nevertheless, traditional epoxy formulations function as passive physical barriers and lack intrinsic capacity to actively impede microbial attachment and proliferation.[22] In contrast, organosilicon materials exhibit a compelling suite of attributes including thermal and oxidative stability, weatherability, hydrophobicity, and dielectric properties which, upon incorporation into epoxy matrices, can alleviate internal stresses, augment toughness, and enhance resistance to aqueous and solvent-borne species.[23–25] Crucially, the initiation of MIC hinges upon bacterial adhesion and subsequent biofilm formation, as only sessile, surface-associated cells not their planktonic counterparts are capable of extracting electrons directly from metallic substrates. In this context, surface hydrophilicity and roughness are recognized as pivotal determinants modulating bacterial attachment.[26,27] It is well established that surfaces enriched with $-CF_3$ moieties minimize surface free energy, and the introduction of organofluorine constituents imparts pronounced hydrophobicity and oleophobicity.[28] Thus, the rational design of fluorosilicone-modified epoxy organic antimicrobial coatings not only erects a formidable barrier between the metal and the corrosive milieu but also actively impairs microbial adhesion, constituting a critical pathway toward realizing proactive antimicrobial functionality.

Recent advances in nanotechnology have opened new avenues for microbial inhibition, with silver nanoparticles (Ag NPs) attracting considerable interest due to their intrinsic physicochemical properties and broad-spectrum antimicrobial activity.[29] Mechanistically, direct contact with bacterial membranes compromises membrane integrity, causing leakage of intracellular constituents, while the sustained release of Ag^+ ions binds to membrane proteins and enzymatic thiol groups, generating reactive oxygen species (ROS) that induce lethal oxidative damage.[30–34] However, the direct incorporation of Ag NPs into coating formulations is often hindered by agglomeration, sedimentation, and phase separation, which severely limit practical efficacy. To address this bottleneck, we employ an aminosilane coupling agent to functionalize the Ag NP surface. Hydrolysis and condensation of the aminosilane generate a protective organosilica shell around each nanoparticle.[35,36] This core–shell architecture serves multiple critical functions: (i) it markedly enhances compatibility and dispersion stability within the hydrophobic epoxy–fluorosilicone matrix *via* the principle of "like dissolves like"; (ii) the silica shell acts as a controlled-release barrier, modulating Ag^+ ion diffusion to enable sustained antimicrobial activity;[37] and (iii) the pendant amine groups provide reactive sites for potential interfacial interaction with the resin matrix, improving adhesion and load transfer.[38,39] Informed by prior studies which including the functionalization of Ag NPs with PUL to impart bactericidal efficacy against *Escherichia coli* and *Staphylococcus aureus*,[40] and the use of amino-fluorosilicone resins as epoxy curing agents that preserve corrosion resistance while mitigating brittleness,[41] we adopt a "cladding" strategy wherein surface-modified Ag NPs ensure uniform dispersion and long-term stability within the organic phase. Moreover, encapsulation within the organosilica layer confers a sustained-release effect: as the coating undergoes microbial erosion, the embedded Ag NPs are progressively exposed, thereby effectuating persistent bactericidal action.[42]

Informed by these design principles, this study details the formulation of a novel composite coating that integrates aminosilicone-encapsulated silver nanoparticles (SNA) with an amino-fluorosilicone curing agent within a bisphenol A-type epoxy matrix, thereby endowing the resulting material with integrated hydrophobic, oleophobic, antimicrobial, and anticorrosive properties. The incorporation of the fluorosilicone resin confers multiple synergistic advantages: (i) it ensures efficient crosslinking and curing of the epoxy base; (ii) the integration of flexible fluorosilicone segments alleviates the intrinsic rigidity of the epoxy network, thereby enhancing coating toughness and flexibility;[43,44] and (iii) the surface enrichment of high-density C–F bonds markedly reduces the overall surface energy, imparting exceptional water- and oil-repellency as well as self-cleaning characteristics that effectively deter microbial adhesion and subsequent fouling. Moreover, the high bond energy and steric shielding afforded by the C–F linkages fortify the chemical and corrosion resistance of the coating. In contrast to the performance benchmarks mandated for extant aviation fuel tank linings (*e.g.*, impact resistance per GB/T 34202-2017 and ISO 7186:2011, and chemical inertness toward prolonged immersion in aggressive media), pristine epoxy coatings still exhibit shortcomings in thermal stability and long-term barrier performance. Accordingly, this investigation seeks to transcend the limitations of conventional epoxy coatings for aviation fuel storage and transport applications through the synergistic interplay of silver nanoparticle-mediated bactericidal activity and fluorosilicone-derived antifouling attributes. We provide a comprehensive evaluation of the corrosion resistance of the developed coating in acidic, alkaline, and saline fog environments, alongside a systematic assessment of its antimicrobial efficacy against *Escherichia coli*, *Staphylococcus aureus*, and SRB, thereby presenting a durable, high-performance strategy for mitigating MIC in demanding operational settings.

2. Materials and methods

2.1 Materials

γ-Aminopropyltriethoxysilane (KH550, industrial grade) and diphenyldimethoxysilane (DMDPS, industrial grade) were obtained from Hangzhou Dadi Chemical Co., Ltd.

Tridecafluorooctyltrimethoxysilane (PFOTS, industrial grade) was purchased from Shushu Dongye Chemical Technology Co., Ltd. Diethoxysilane (DMDES, industrial grade) was supplied by Nanjing Yupu Chemical Co., Ltd. Dibutyltin dilaurate (DBTDL, analytical grade) was acquired from Tianjin Kemo Chemical Reagent Co. Bisphenol A diglycidyl ether (E51, industrial grade) and polyether amine curing agent (D230, industrial grade) were procured from Shaanxi Tianyuan Synthesis Co., Ltd. Tetraethyl orthosilicate (TEOS, analytical grade) was sourced from Sinopharm Chemical Reagent Co., Ltd. Silver nanoparticles (analytical grade) were obtained from Beijing Dekdojima Gold Technology Co., Ltd. Anhydrous ethanol (analytical grade) was supplied by Tianjin Hedong Hongyan Reagent Factory. *Desulfovibrio desulfuricans* (SRB, strain 1.5190) was purchased from the China General Microorganism Culture Collection and Management Center. Components for SRB culture medium were sourced from Macklin Biochemical Co., Ltd (China); detailed preparation protocols are provided in the SI (section S1).

2.2 Preparation of SNA

Amino-modified silica-encapsulated silver nanoparticles (denoted as SNA) were synthesized *via* a sol–gel co-condensation process. Silver nanoparticles (0.5 g) were dispersed in a mixed solvent of ethanol (7.5 g) and water (7.5 g) under mechanical stirring at 500 rpm. The suspension was heated to 70 °C. Subsequently, a pre-mixed precursor solution containing 16.67 g TEOS and 4.43 g KH550 (TEOS : KH550 molar ratio = 2 : 1) was added dropwise over 2 h (approximately one drop per 3 seconds). Following the addition, the reaction was continued at 70 °C for 15 h, yielding a pale-yellow solution. The product was isolated by drying the resultant solution at 120 °C, and the obtained solid was ground into a fine powder to afford the final SNA material (Fig. 1).

2.3 Preparation of FPS

FPS resin was synthesized by the catalyzed co-condensation of silane monomers. KH-550 (26.56 g), DMDPS (29.32 g), DMDES (17.79 g), and PFOTS (7.37 g) (molar ratio 1 : 1 : 1 : 0.13) were combined in a flask and heated to 80 °C with stirring (500 rpm). Dibutyltin dilaurate (DBTDL, 0.24 g) was added as a catalyst, followed by the dropwise addition of deionized water (15.97 g) at 7.51 mL min^{-1}. The mixture was stirred under reflux at 80 °C for 6 h. The resulting pale-yellow liquid was then rotary-evaporated to remove volatile alcohols, yielding the amino-fluorosilicone resin (FPS) as a transparent product (Fig. 2).

2.4 Preparation of SNA-FPS/ER coatings

The SNA-FPS/ER coatings were prepared by the following procedure. First, the SNA-FPS component was obtained by mixing the amino-fluorosilicone resin (FPS), the SNA powder, and the polyetheramine D230. This component was then combined with the epoxy resin (E51) and the relevant nanofillers. The

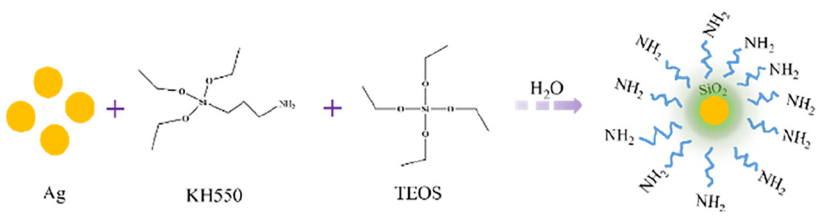

Fig. 1 Synthesis of SNA.

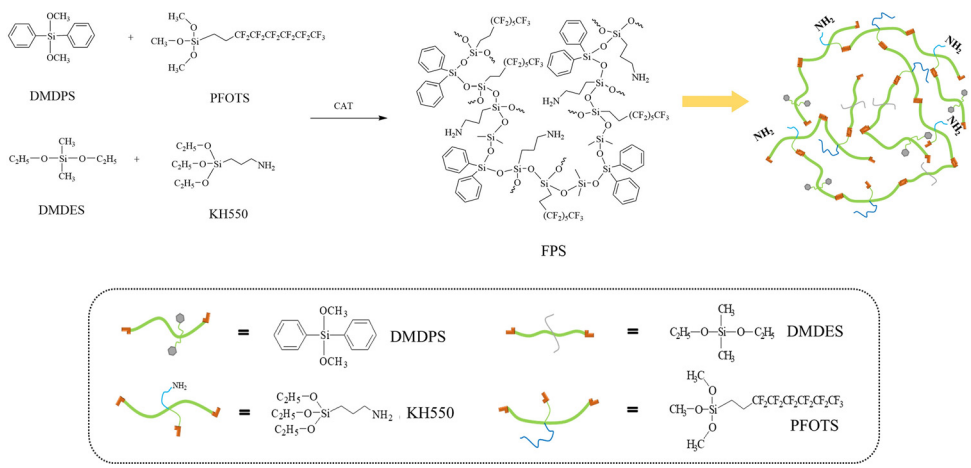

Fig. 2 Synthesis of FPS.

Table 1 Coating formula

Name	wt%
SNA	0–4
FPS	50–100
D230	10–15
E51	80–100
TiO_2	65–100
Dispersing and wetting agent	2–4
Anti-foam	2–4
Ethyl acetate	30–55
Toluene	20–35

specific formula is shown in Table 1. The mixture was homogenized using a high-speed disperser, degassed under vacuum, and subsequently applied onto polished tinplate substrates. The coatings were cured with a two-stage thermal treatment: 70 °C for 30 min and 120 °C for 30 min.

The FPS/ER matrix was selected as the foundation for the composite coatings, with SNA incorporated at contents of 0%, 0.5%, 1%, 1.5%, and 2%, respectively. These composite coatings were designated as FPS/ER, SNA-FPS/ER-1, SNA-FPS/ER-2, SNA-FPS/ER-3, and SNA-FPS/ER-4, respectively (Fig. 3).

2.5 Characterization studies

Fourier-transform infrared (FTIR) spectroscopy of the FPS resin was performed on a spectrometer in the range of 4000–500 cm^{-1}. ^1H nuclear magnetic resonance (^1H NMR) spectroscopy was conducted using a deuterated chloroform ($CDCl_3$) solution with tetramethylsilane (TMS) as an internal standard. The morphology of the SNA particles was observed by transmission electron microscopy (TEM; model Tecnai G2 F20 S-TWIN). For TEM sample preparation, a droplet of a 0.1 wt% SNA dispersion, negatively stained with 2 wt% phosphotungstic acid, was placed on a carbon-coated copper grid and air-dried. Dynamic light scattering (DLS) and zeta potential measurements were carried out on a Zetasizer Nano-ZS90 instrument. The SNA sample was diluted to 1 wt% with deionized water for DLS analysis. Meanwhile, the morphology of the coatings was examined by scanning electron microscopy (SEM) and atomic force microscopy (AFM). Surface elemental analysis was performed using X-ray photoelectron spectroscopy (XPS). The crystallinity of the samples was assessed by X-ray diffraction (XRD) over a 2θ range of 5° to 60°.

The physicochemical and functional properties of the composite coatings were systematically characterized. The water contact angle (WCA) was measured at ambient temperature using an optical contact angle goniometer (OCA20) to evaluate surface wettability. Mechanical properties including adhesion (cross-cut test), pencil hardness, impact resistance, and flexibility (conical mandrel bend test) were evaluated in accordance with relevant Chinese National Standards (ISO 7619-1&ASTM D2240, GB/T 9286-2021/ISO 2409:2020, GB/T 9274-1988, GB/T 1771-2007). The chemical resistance was assessed by exposing the coated panels to acidic, alkaline, and neutral salt spray environments as per standard protocols. The electrochemical corrosion behavior of the SNA-FPS/ER coatings was investigated using a CHI 660B electrochemical workstation. Both electrochemical impedance spectroscopy (EIS) and potentiodynamic polarization (Tafel) measurements were conducted in a 3.5 wt% NaCl aqueous solution to obtain insights into the corrosion protection mechanisms and rates. The antimicrobial efficacy of the coatings was quantitatively assessed against representative Gram-negative (*Escherichia coli*), Gram-positive (*Staphylococcus aureus*), and anaerobic corrosive (*Desulfovibrio vulgaris*, a model sulfate-reducing bacterium, SRB) strains, following established shake-flask or biofilm assay methods.

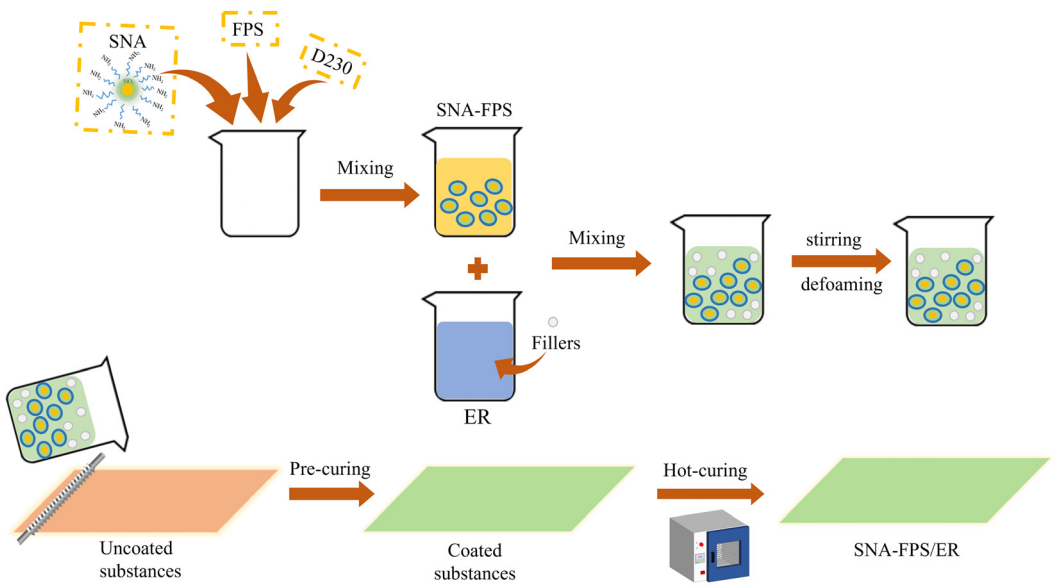

Fig. 3 Construction route of SNA-FPS/ER coatings.

3 Results and discussion

3.1 Characterization of FPS

The FPS was characterized as a yellowish, transparent, viscous liquid with a viscosity of 1200 mPa s and a refractive index of 1.5148. FTIR (cm^{-1}): 3660–3238 (s, ν_{Si-OH}, ν_{N-H}), 3047 (w, δ_{Ar-H}, C_6H_6), 2960–2871 (m, ν_{C-H}), 1660–1425 (w, $\delta_{C=C}$, C_6H_6), 1249 (m, ν_{C-F}), 1120 (s and wide, ν_{Si-O}), 1064 (s, ν_{C-N}), 698 (m, ν_{-NH2}). ^{1}H-NMR (δH): 0.14 (d, aH, Si–CH_3), 0.86 (s, bH, $SiCH_2$–), 1.32 (m, cH, Si–CH_2–CH_2–), 2.02 (s, dH, $CF_3(CF_2)_5$–CH_2–), 2.67 (s, eH, –NH_2), 3.46 (s, fH, Si–OH), 3.69 (d, gH, NH_2–CH_2–), 7.34 (t, hH, Si-Ph). Both FTIR and NMR characterization studies confirmed that the FPS was consistent with the expected design structure (Fig. 4).

3.2 Characterization of SNA

As shown in Fig. 5a, the as-synthesized solvent-borne SNA dispersion, although optically transparent, contains a high density of uniformly dispersed spherical nanoparticles. The inset further confirms the preservation of a well-defined solid spherical morphology following solvent removal. Fig. 5b displays the corresponding particle size distribution and zeta potential of the SNA dispersion. The nanoparticles exhibit a mean hydrodynamic diameter of approximately 104 nm and a zeta potential ranging from −38.7 mV to −72.4 mV, with an average value of −50.7 mV. The uniformly negative surface charge across the nanoparticle population induces electrostatic repulsion between adjacent particles, effectively suppressing interparticle attraction and aggregation, thereby imparting enhanced colloidal stability. Fig. 5c presents a representative TEM image of 0.1 wt% SNA negatively stained with phosphotungstic acid. The micrograph reveals the core–shell architecture of SNA, wherein silver nanoparticles are encapsulated within a KH550-derived organic matrix. Observations conducted at magnifications of 8×10^3 (scale bar = 2 μm) and 1.4×10^5 (scale bar = 200 nm) demonstrate that SNA effectively introduces silver as a potent and stable biocide into the system, with the KH550 shell facilitating uniform dispersion

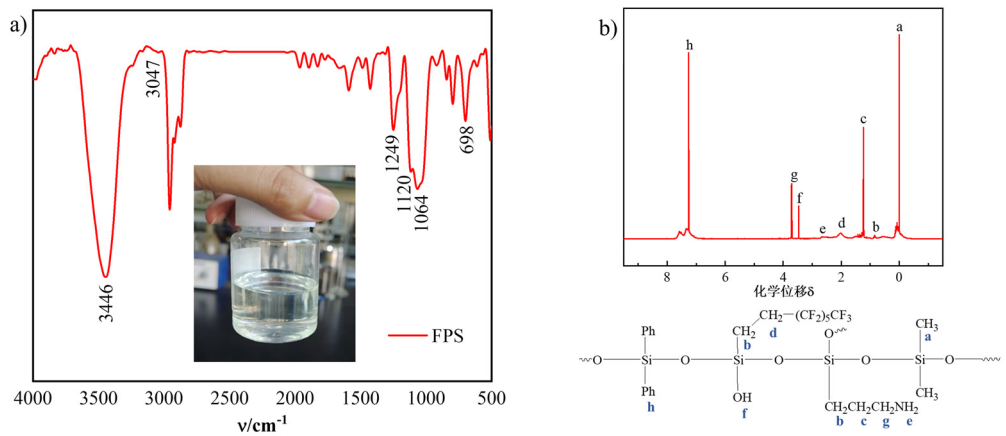

Fig. 4 (a) FTIR of FPS. (b) ^{1}H NMR of FPS.

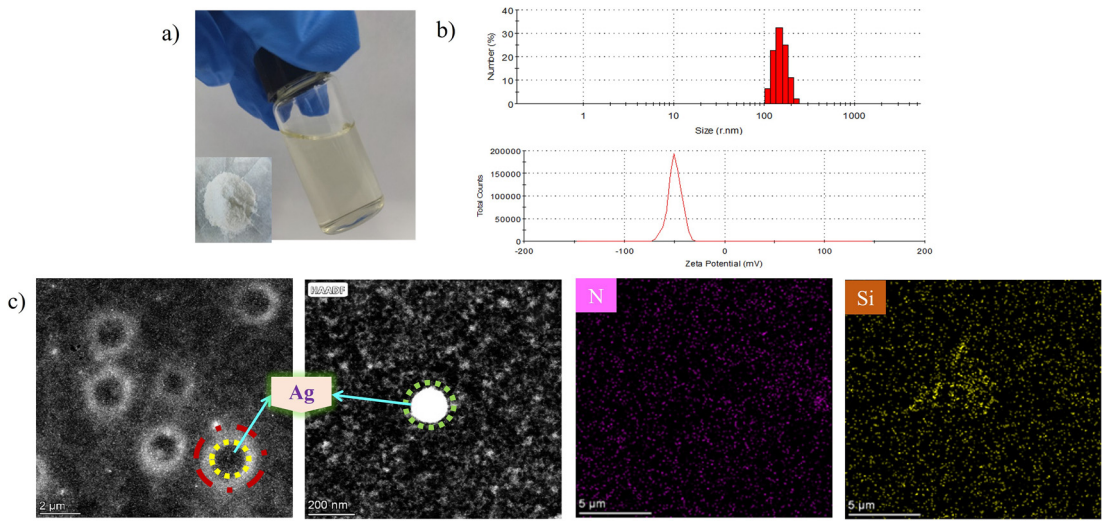

Fig. 5 (a) Solid and liquid maps of SNA, (b) particle size distribution of SNA and (c) TEM characterization of SNA.

of the Ag cores. This core–shell configuration not only mitigates the inherent tendency of nanosilver to sediment in organic media but also establishes a sustained-release antimicrobial reservoir.

3.3 Surface morphology and elemental analysis of SNA-FPS/ER coatings

Fig. 6a presents the X-ray diffraction patterns of the pristine silver nanoparticles, the FPS/ER coating, and the SNA-FPS/ER-2 composite coating. The silver nanoparticles exhibit distinct diffraction peaks at 2θ values of 38.12°, 44.28°, 64.43°, and 77.47°, which correspond respectively to the (111), (200), (220), and (311) crystallographic planes of face-centered cubic silver (JCPDS no. 04-0782). Both the FPS/ER and SNA-FPS/ER-2 coatings display a broad amorphous halo centered at approximately 2θ = 19.36°, characteristic of the siloxane (Si–O–Si) network. Notably, the diffraction pattern of SNA-FPS/ER-2 additionally exhibits sharp crystalline reflections at 2θ = 38.04°, 44.36°, 64.48°, and 77.44°, which closely match the positions and profiles of the silver nanoparticle reflections. This congruence unequivocally confirms the successful incorporation of silver nanoparticles within the coating matrix.

Fig. 6b displays the X-ray photoelectron spectroscopy (XPS) surface elemental analysis of the SNA-FPS/ER-2 coating. As shown in Fig. 6b$_1$, the coating surface comprises six elements – Si, C, Ag, N, O, and F with relative atomic concentrations of 6.89%, 63.14%, 0.46%, 3.15%, 16.62%, and 9.74%, respectively. The corresponding Si 2p, C 1s, Ag 3d, N 1s, O 1s, and F 1s core-level signals are centered at binding energies of 102.08 eV, 284.08 eV, 367.08 eV, 399.08 eV, 532.08 eV, and 689.08 eV. The high-resolution Ag 3d spectrum (Fig. 6b$_2$) exhibits two distinct spin–orbit components: the Ag 3d$_{5/2}$ peak at 368.28 eV and the Ag 3d$_{3/2}$ peak at 374.18 eV. These observations corroborate the successful incorporation of SNA into the coating matrix.

Fig. 6c and d present scanning electron microscopy (SEM) and atomic force microscopy (AFM) images of the FPS/ER and SNA-FPS/ER coatings, respectively. The SEM micrograph of FPS/ER (Fig. 6c$_1$) reveals a predominantly smooth, featureless surface, consistent with the continuous film morphology formed during resin curing. In contrast, the SNA-FPS/ER coating (Fig. 6c$_2$) exhibits a surface decorated with uniformly distributed spherical protrusions of comparable dimensions, attributable to the incorporation of SNA nanoparticles. Fig. 6d$_1$ and d$_2$ (3D figure of AFM) further illustrate this morphological transition from a relatively planar architecture to a textured topography characterized by groove-like elevations, indicative of increased surface roughness. Quantitative rough-

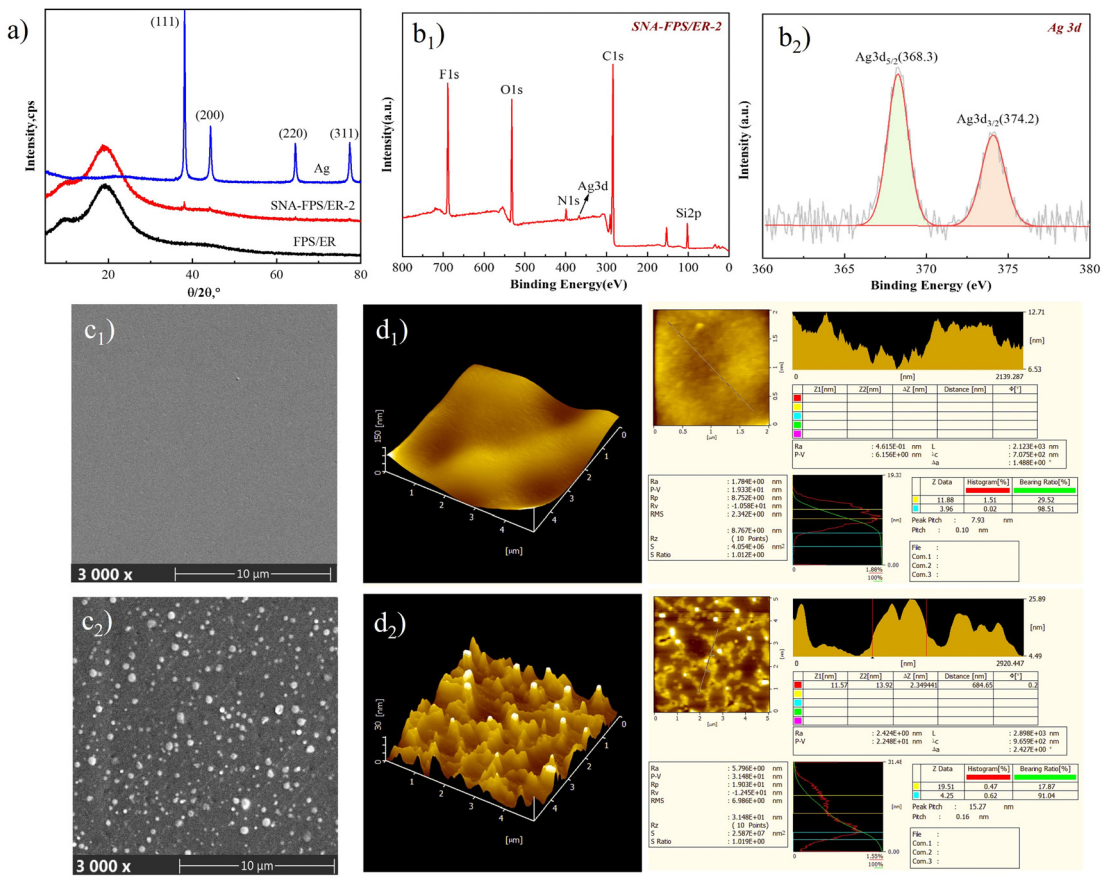

Fig. 6 (a) XRD of Ag, FPS-ER, and SNA-FPS/ER. (b) XPS of coatings: (b$_1$) full spectrum, (b$_2$) high-resolution spectrum of Ag 3d. (c) SEM of coatings: (c$_1$) FPS/ER, (c$_2$) SNA-FPS/ER. (d) AFM of coatings: (d$_1$) 3D and 2D figures of FPS/ER, (d$_2$) 3D and 2D figures of SNA-FPS/ER.

ness analysis derived from the two-dimensional AFM height profiles yields an arithmetic mean roughness (R_a) value of 1.784 nm for FPS/ER, which increases to 5.796 nm for the SNA-FPS/ER coating. This augmentation in surface roughness is directly ascribed to the introduction of SNA nanoparticles, which generate a lotus-leaf-inspired nanoscale protrusion morphology that contributes to enhanced hydrophobicity. Moreover, the encapsulation of the silver cores within the KH550-derived organic layer not only promotes homogeneous nanoparticle dispersion throughout the coating matrix but also facilitates the sustained release of biocidal silver species, thereby imparting durable antibacterial and bactericidal functionality to the composite coating.

3.4 Mechanical properties and chemical resistance of the SNA-FPS/ER composite coatings

The physical and mechanical properties of the SNA-FPS/ER composite coatings are summarized in Table 2. All formulations exhibited excellent adhesion, consistently rated as grade 1, together with a modest increase in pencil hardness. The static water contact angle (WCA) displayed a non-monotonic trend, initially rising from 109° to a maximum of 115° at an SNA loading of 1 wt%, followed by a slight decline upon further SNA incorporation. This behavior is attributed to the introduction of SNA nanoparticles, which augment surface roughness and thereby enhance hydrophobicity. At higher SNA loadings, however, nanoparticle agglomeration within the matrix becomes more prevalent, leading to a reduction in surface uniformity and a corresponding decrease in WCA. As demonstrated in Table 3 and Fig. 7, the inclusion of SNA does not appreciably compromise the chemical resistance of the composite coatings. No significant deterioration of the coating surfaces was observed following exposure to acidic, alkaline, saline spray, or oil-based environments, confirming that the SNA-FPS/ER composites retain adequate chemical durability under the evaluated conditions.

3.5 Electrochemical corrosion resistance of SNA-FPS/ER composite coatings

To rigorously evaluate the coating performance in biologically relevant corrosive scenarios, electrochemical tests were conducted in both a standard 3.5 wt% NaCl solution and a solution simulating the metabolic environment of sulfate-reducing bacteria (SRB, containing 10^{-3} M H_2S). The key results are presented in Fig. 8 and Table 4.

The Bode magnitude plot (Fig. 8a) shows that the impedance modulus in the low-frequency region, a direct indicator of coating protection capability, is drastically improved by SNA incorporation. The optimal formulation (SNA-FPS/ER-2, 1 wt% SNA) exhibits a $|Z|_{0.01\ Hz}$ value of $5 \times 10^4\ \Omega\ cm^2$, which is over four times higher than that of the SNA-free FPS/ER coating. The Nyquist plots (Fig. 8b), characterized by a single, depressed capacitive loop, further support this finding. The diameter of this loop, proportional to the polarization resistance, expands significantly with 1 wt% SNA addition, indicating superior resistance to charge transfer associated with the corrosion reaction.

The performance variation with SNA content follows a clear volcano trend. The initial enhancement is attributed to the well-dispersed SNA nanoparticles acting as impermeable fillers, which increase the tortuosity of the diffusion path for corrosive species and block inherent micro-pores in the polymer matrix. At the optimal 1 wt% loading, the coating achieves maximum densification. However, beyond this critical concentration, nanoparticle agglomeration becomes prevalent. These agglomerates act as defects, compromising the polymer–filler interface and potentially creating preferential pathways for electrolyte penetration, which explains the subsequent decrease in impedance. This comprehensive analysis confirms that the corrosion resistance of the SNA-FPS/ER composite coating is non-linearly dependent on the SNA loading, with 1 wt% identified as the optimal concentration for achieving synergistic matrix densification and sustained barrier functionality.

Table 2 Physical properties of SNA-FPS/ER composite coatings

Sample	Adhesion/grade	Impact resistance/kg cm	Flexibility/cm	Pencil hardness/H	WCA/°
FPS/ER	1	30	2.0	4 H	105
SNA-FPS/ER-1	1	≥50	1.0	5 H	113
SNA-FPS/ER-2	1	≥50	1.0	5 H	118
SNA-FPS/ER-3	1	≥50	0.5	5 H	125
SNA-FPS/ER-4	1	≥50	0.5	5 H	125

Table 3 Chemical corrosion resistance of SNA-FPS/ER composite coatings

Sample	H_2SO_4 (wt 5%)/168 h	NaOH (wt 5%)/168 h	NaCl (wt 5%)/720 h	Jet fuel/168 h
FPS/ER	No change	No change	Erosion at scratches ≤ 2 mm	No change
SNA-FPS/ER-1	No change	No change	Erosion at scratches ≤ 2 mm	No change
SNA-FPS/ER-2	No change	No change	Erosion at scratches ≤ 2 mm	No change
SNA-FPS/ER-3	No change	No change	Erosion at scratches ≤ 2 mm	No change
SNA-FPS/ER-4	No change	No change	Erosion at scratches ≤ 2 mm	No change

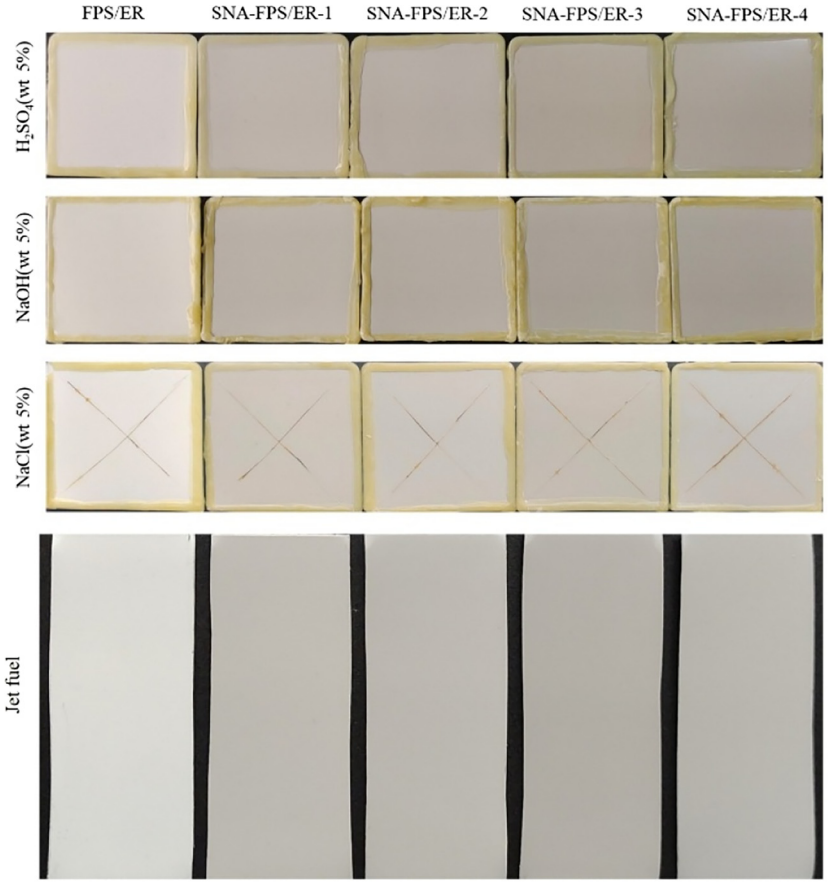

Fig. 7 Chemical corrosion resistance of SNA-FPS/ER composite coatings.

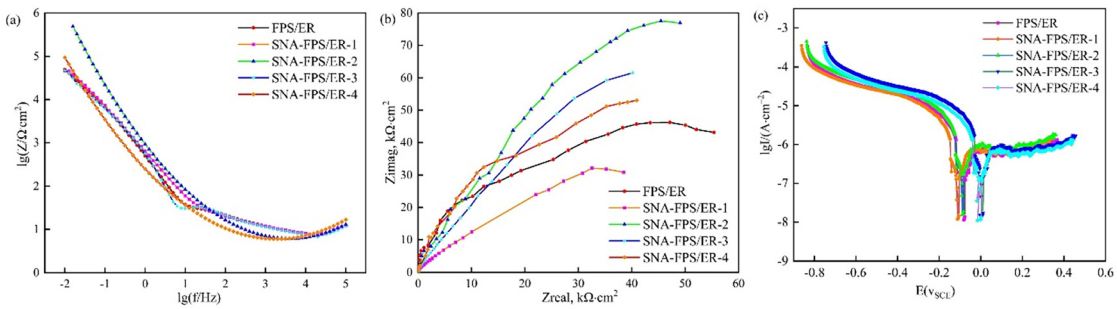

Fig. 8 Electrochemical corrosion of SNA-FPS/ER: (a) Bode, (b) Nyquist, and (c) Tafel.

Table 4 Tafel curve fitting data of SNA-FPS/ER composite coatings

Sample	E_{corr}/V	I_{corr}/A cm^{-2}	Corrosion rate/mm a^{-1}
FPS/ER	−0.0788	1.21×10^{-8}	0.288×10^{-3}
SNA-FPS/ER-1	−0.108	3.21×10^{-7}	0.393×10^{-3}
SNA-FPS/ER-2	−0.0849	7.35×10^{-8}	0.302×10^{-3}
SNA-FPS/ER-3	0.00890	7.32×10^{-7}	0.345×10^{-3}
SNA-FPS/ER-4	0.00491	6.16×10^{-7}	0.328×10^{-3}

As shown in Fig. 8c and summarized in Table 4, with increasing SNA loading, the corrosion potential of the composite coating exhibits a non-monotonic trend—first decreasing and then rising—while the corrosion current density follows an inverse trajectory, initially decreasing before increasing. Consequently, the corrosion rate displays a minimum at intermediate SNA content. This behavior confirms that the dispersion state of SNA directly governs the corrosion resistance of the composite coating. Optimal dispersion is achieved at 1 wt% SNA loading, corresponding to a corrosion potential of

−0.0849 V, a corrosion current density of 7.35×10^{-8} A cm^{-2}, and a corrosion rate of 0.302×10^{-3} mm a^{-1}, at which point the coating affords maximal protection. In the absence of SNA, barrier properties arise solely from the crosslinked, irregular network formed by the fluorosilicone-modified epoxy resin. When SNA is introduced at levels exceeding 1 wt%, corrosion inhibition is mediated first by SNA particles localized at the coating surface, followed by the bulk of the hybrid composite. This sequence accounts for the observed shifts in corrosion potential, the reduction in current density, and the diminished corrosion rate. Collectively, the Tafel polarization data are fully consistent with the Bode and Nyquist analyses, corroborating that the SNA-FPS/ER composite coating containing 1 wt% SNA delivers robust corrosion protection for the underlying substrate.

3.6 Antimicrobial performance test of SNA-FPS/ER composite coatings and research on the antimicrobial mechanism

Silver nanoparticles (Ag NPs) are well-known for their broad-spectrum antimicrobial properties, which are mainly attributed to the release of Ag^+ ions that interfere with essential bacterial enzymes and cellular processes. To impart these properties to the epoxy-fluorosilicone coating, aminosilane-encapsulated Ag NPs (SNA) were incorporated into the FPS/ER formulation. The antimicrobial performance of the resulting SNA-FPS/ER composite coatings was then experimentally determined using the plate counting method.

Table 5 Antimicrobial rate of SNA-FPS/ER composite coatings against *E. coli* and *S. aureus*

		Antimicrobial rate/%	
Sample	SNA/%	*E. coli*	*S. aureus*
Blank group	0	0	0
FPS/ER	0	59.5	62.3
SNA-FPS/ER-1	0.5	93.3	94.7
SNA-FPS/ER-2	1	99.54	99.63
SNA-FPS/ER-3	1.5	99.99	99.99
SNA-FPS/ER-4	2	99.99	99.99

The antibacterial performance of the composite coatings is presented in Table 5 and Fig. 9. The data show the bacterial survival counts and calculated bactericidal rates for coatings with varying SNA loadings after a 24-hour exposure to *E. coli* and *S. aureus*. All tests were conducted with reference to a blank control group.

The antibacterial efficacy, presented in Fig. 9 and Table 4, reveals a clear positive correlation between SNA loading and antimicrobial performance. Visual inspection of the agar plates (Fig. 9) indicates that while the uncoated reference and the pristine FPS/ER coating allowed for substantial bacterial survival and proliferation, the SNA-FPS/ER composites significantly inhibited growth. This inhibitory effect was markedly enhanced as the SNA concentration increased. The corresponding quantitative bactericidal rates (Table 4) substantiate this observation. The composite with 0.5 wt% SNA (SNA-FPS/ER-1) inactivated ≥93% of both *E. coli* and *S. aureus*. Further increasing the SNA content to 1–2 wt% (SNA-FPS/ER-3 and -4) elevated the bactericidal rate to 99–99.99%, indicating that at optimal loadings, the coating surface possesses near-sterilizing properties. These results unequivocally demonstrate that the incorporation of SNA nanoparticles is highly effective in endowing the epoxy-fluorosilicone coating with potent, dosage-dependent antimicrobial functionality.

As presented in Fig. 10, the antibacterial efficacy of the coatings demonstrates a definitive composition-dependent trend. The unmodified FPS/ER coating showed a bactericidal rate of only about 60%, reflecting its passive, non-biocidal nature. The introduction of SNA nanoparticles transformed this performance, with efficacy increasing monotonically with SNA content. The bactericidal rate surpassed 93% at 1 wt% loading and achieved >99.5% at 2 wt%, indicating near-sterilizing surface properties at optimal loadings. This remarkable improvement is rationalized by a dual mechanism. First, the aminosilane-encapsulated Ag NPs (SNA) provide a reservoir for Ag^+ ions, which are released upon contact with moisture and microbial metabolites. These ions inactivate bacteria by disrupting enzymatic and structural proteins. Second, the fluorosilicone-modified resin matrix creates a hydrophobic, low-

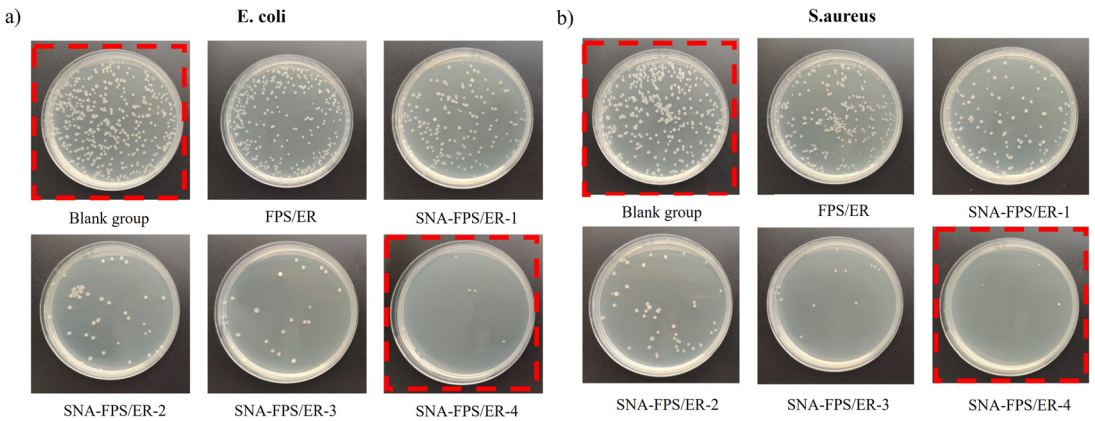

Fig. 9 Macroscopic view: (a) *E. coli* colony count and (b) *S. aureus* colony count.

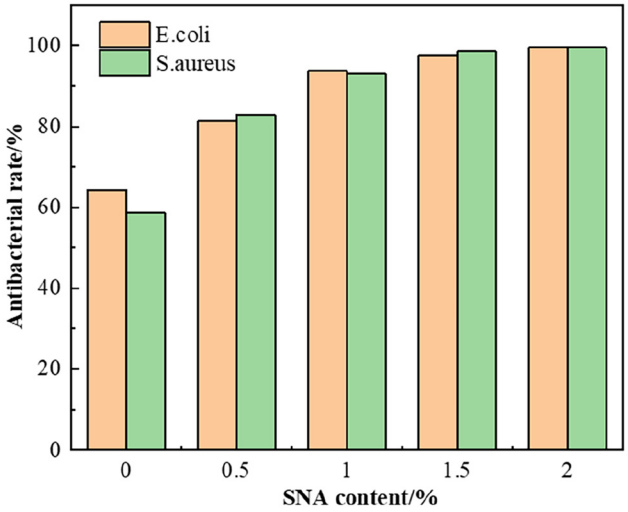

Fig. 10 Antibacterial rate of SNA-FPS/ER composite coatings.

surface-energy surface that minimizes the thermodynamic driving force for bacterial attachment. The synergistic effect between this anti-adhesion property and the active biocidal function of SNA explains the composite coating's outstanding and durable antimicrobial performance.

Sulfate-reducing bacteria (SRB) are key contributors to biocorrosion in industrial systems through their sulfide-producing metabolism. The development of coatings resistant to SRB is therefore crucial for infrastructure protection. To evaluate the SRB-inhibiting performance of the SNA-FPS/ER composite coating developed in this work, a standardized laboratory corrosion test was conducted. Coating specimens were immersed in an active SRB suspension for 7 days. Subsequently, the surfaces were examined to assess microbial adhesion, biofilm formation, and any induced corrosion damage. The comparative results, which demonstrate the coating's protective effect, are shown in Fig. 11.

The long-term resistance of the SNA-FPS/ER coatings to sulfate-reducing bacteria (SRB)-induced corrosion was rigorously evaluated. Coating samples with varying SNA contents (0.5, 1, 1.5, and 2.0 wt%) were immersed in an active SRB culture (concentration $\approx 10^4$ CFU mL^{-1}) at 37 °C for 7 days, simulating a highly aggressive microbial environment. As shown in Fig. 11, all SNA-containing coatings (SNA-FPS/ER-1 to -4) maintained their structural integrity with no visible signs of corrosion, pitting, or biofilm-induced discoloration. In stark contrast, the control FPS/ER coating (without SNA) exhibited a distinct pinkish hue and severe surface blistering, which are characteristic indicators of active SRB corrosion and acidic metabolite attack (*e.g.*, H_2S and H_2SO_4).

This exceptional performance is attributed to the synergistic design of the composite. The sustained release of Ag^+ ions from the embedded SNA nanoparticles effectively inactivates SRB at the coating surface, preventing the formation of corrosive biofilms. Concurrently, the hydrophobic, low-surface-energy matrix derived from the fluorosilicone modification acts as a barrier, limiting the adhesion of microorganisms and the ingress of water and aggressive ions. Furthermore, as summarized in Table 6, the key physical properties (*e.g.*, adhesion and hardness) of the SNA-FPS/ER coatings remained virtually unchanged after the 7-day SRB immersion, confirming their exceptional dura-

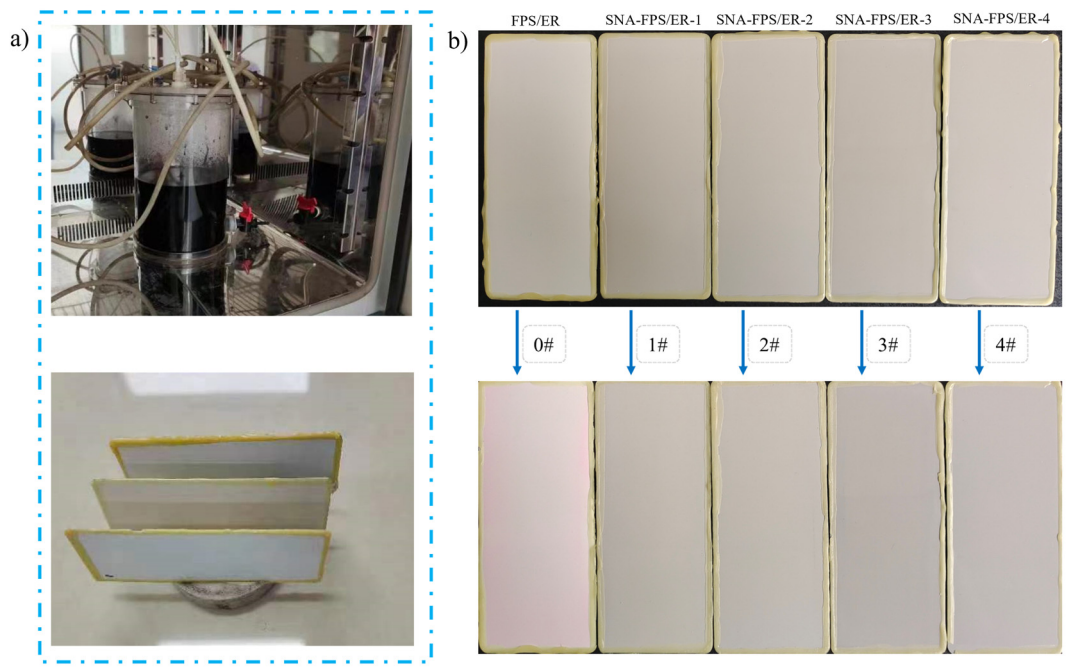

Fig. 11 (a) Schematic diagram of the corrosion sample setup used to test the corrosion resistance of SRB. (b) Optical photo of SNA-FPS/ER composite coatings after 7 days in SRB medium.

Table 6 Physical properties of SNA-FPS/ER composite coatings after SRB immersion for 7 days

Sample	Adhesion/ grade	Flexibility/ cm	Pencil hardness/H	WCA/°
FPS/ER	1	2.0	4 H	103
SNA-FPS/ER-1	1	1.0	5 H	116
SNA-FPS/ER-2	1	1.0	5 H	119
SNA-FPS/ER-3	1	0.5	5 H	121
SNA-FPS/ER-4	1	0.5	5 H	123

bility. These results collectively demonstrate that the SNA-FPS/ER composite coating achieves integrated and durable antimicrobial/anticorrosive functionality through a combined mechanism of active biocide release and passive surface protection.

4 Conclusion

In this study, a multifunctional epoxy composite coating (SNA-FPS/ER) integrating water repellency, oil repellency, long-lasting antimicrobial activity, and high corrosion resistance was successfully fabricated through rational molecular design. The core innovation lies in the synergistic integration of two functional components. First, aminosilane-encapsulated silver nanoparticles (SNA) were synthesized *via* a sol–gel process. The organic shell effectively addressed the critical challenges of dispersion and stability of Ag NPs within the resin matrix, establishing a foundation for controlled, sustained-release antimicrobial functionality. Second, an amino-fluorosilicone resin (FPS) was prepared *via* hydrolytic co-condensation. Serving as both a curing agent and a modifier, it ensured effective cross-linking of the epoxy network (E51) while introducing flexible segments for toughening. The surface enrichment of fluorocarbon chains imparted an ultra-low surface energy to the coating.

Systematic performance evaluation demonstrated that the as-prepared SNA-FPS/ER coatings exhibit outstanding comprehensive properties. The adhesion reached grade 1, pencil hardness was 5H, impact resistance was ≥50 cm, and the coating withstood 1000 hours of immersion in aviation kerosene without blistering, peeling, or wrinkling. Within the SNA content range of 0.5–2.0 wt%, the antimicrobial and anticorrosive performance showed a clear dose-dependent relationship. When the SNA loading was ≥1 wt%, the coating achieved bactericidal rates exceeding 99% against both *E. coli* and *S. aureus*. Electrochemical tests further confirmed that at this optimized loading (*e.g.*, 1 wt% SNA), the low-frequency impedance modulus increased to 5×10^4 Ω cm^2, and the corrosion current density dropped to as low as 7.35×10^{-8} A cm^{-2}, significantly outperforming the unmodified coating. More critically, after 7 days of immersion in a sulfate-reducing bacteria (SRB) solution (10^4 CFU mL^{-1}) at 37 °C, the SNA-containing coatings (particularly with 2 wt% SNA) remained intact with no visible corrosion or biofilm-induced discoloration, while the control sample exhibited severe pitting and blistering. This strongly validates the long-term durability of the coating in a simulated, realistic biocorrosion environment.

In summary, this work employs a synergistic strategy combining "aminosilane-encapsulated silver nanoparticles" and "fluorosilicone-modified epoxy." This approach not only overcomes the technical bottlenecks of poor dispersion and single functionality of nanofillers in polymers but also successfully produces a high-performance protective coating suitable for demanding environments such as aviation fuel storage and transportation systems. This study provides a novel perspective and a viable material solution for designing the next generation of polymer-based composite materials with active-passive dual-protection mechanisms.

Conflicts of interest

There are no conflicts to declare.

Data availability

All data supporting the findings of this study are available within the article and its supplementary information (SI). Supplementary information is available. See DOI: https://doi.org/10.1039/d5py01145k.

No external datasets were generated or analyzed beyond those presented.

Acknowledgements

This work was supported by the Sci-tech Innovation Team of Shaanxi Province (2024RS-CXTD-46).

References

1 D. Pruski, *et al.*, Jet Fuel Contamination: Forms, Impact, Control, and Prevention, *Energies*, 2024, **17**, 4267, DOI: 10.3390/en17174267.
2 X. Lv, *et al.*, The Microbiologically Influenced Corrosion and Protection of Pipelines: A Detailed Review, *Materials*, 2024, **17**, 4996, DOI: 10.3390/ma17204996.
3 M. O. Pamula, *et al.*, Preliminary corrosion prevention of microbiologically induced corrosion in high producer main oil pipelines to hinder reoccurrence leak, *Results Eng.*, 2024, **21**, 101972, DOI: 10.1016/j.rineng.2024.101972.
4 L. Xu, *et al.*, "Corrosion-resistant" chromium steels for oil and gas pipelines can suffer from very severe pitting corrosion by a sulfate-reducing bacterium, *J. Mater. Sci. Technol.*, 2024, **174**, 23–29, DOI: 10.1016/j.jmst.2023.01.008.
5 C. Ortega-Nieto, *et al.*, Metal Bionanohybrids against Microbiologically Influenced Corrosion (MIC) Consortia, *Nanomaterials*, 2024, **14**, 1376, DOI: 10.3390/nano14171376.

6 X. Chen, *et al.*, Hydrogen-induced cracking of X70 steel affected by sulfate-reducing bacteria and cathodic potential: experiment and density functional theory study, *Int. J. Hydrogen Energy*, 2024, **49**, 798–810, DOI: 10.1016/j.ijhydene.2023.07.228.
7 I. Santos-Pereda, *et al.*, Effect of Sulphate-Reducing Bacteria Activity on the Performance of Thermally Sprayed Aluminium and Polyurethane Coatings, *Crystals*, 2024, **14**, 260, DOI: 10.3390/cryst14030260.
8 S. He, *et al.*, Comparative analysis of corrosion resistance of pipeline steels exposed to sulfate-reducing bacteria: Insights on L360, L245NS and antibacterial steels, *Int. J. Electrochem. Sci.*, 2025, **20**, 100960, DOI: 10.1016/j.ijoes.2025.100960.
9 N. Liu, *et al.*, Carbon Steel Corrosion Induced by Sulfate-Reducing Bacteria: A Review of Electrochemical Mechanisms and Pathways in Biofilms, *Coatings*, 2024, **14**, 1105, DOI: 10.3390/coatings14091105.
10 L. He, *et al.*, An S2–responsive coating on 70Cu-30Ni alloy for suppressing microbiologically influenced corrosion induced by sulfate-reducing bacteria, *Appl. Surf. Sci.*, 2025, **684**, 161914, DOI: 10.1016/j.apsusc.2024.161914.
11 G. Xing, *et al.*, Intelligent antibacterial coatings based on sensitive response and periodic fast drug release for long-term defense against corrosion induced by sulfate-reducing bacteria, *J. Colloid Interface Sci.*, 2025, **684**, 331–345, DOI: 10.1016/j.jcis.2025.01.040.
12 D. Wang, *et al.*, Eco-friendly bifunctional antibacterial and anticorrosive broad-spectrum rosin thiourea iminazole quaternary ammonium salt against microbiologically influenced corrosion, *Corros. Sci.*, 2024, **229**, 111847, DOI: 10.1016/j.corsci.2024.111847.
13 D. Xia, *et al.*, Understanding the mechanisms behind the antibacterial activity of magnesium hydroxide nanoparticles against sulfate-reducing bacteria in sediments, *Sci. Rep.*, 2024, **14**, 21831, DOI: 10.1038/s41598-024-72516-7.
14 M. Jafari, *et al.*, Corrosion behavior of predominant Halodesulfovibrio in a marine SRB consortium and its mitigation using ZnO nanoparticles, *Sci. Rep.*, 2024, **14**, 19545, DOI: 10.1038/s41598-024-70654-6.
15 V. M. Udowo, *et al.*, Sulfate-Reducing Bacteria Corrosion of Pipeline Steel in Polyacrylamide Gel Used for Enhanced Oil Recovery, *J. Mater. Eng. Perform.*, 2023, **33**, 1114–1129, DOI: 10.1007/s11665-023-08058-2.
16 S. Zhang, *et al.*, Evaluation of the antimicrobial corrosion properties of electropolymerized poly(aniline-co-o-toluidine) films on carbon steel surfaces, *Synth. Met.*, 2025, **311**, 117812, DOI: 10.1016/j.synthmet.2024.117812.
17 Y. Meng, *et al.*, Preparation and Characterization of Low Surface Energy Waterborne Acrylic Anticorrosion and Antibacterial Coatings Applied in Maritime Protection, *ACS Appl. Polym. Mater.*, 2025, **7**, 1307–1317, DOI: 10.1021/acsapm.4c03002.
18 R. Liu, *et al.*, Gallic acid-modified montmorillonite reinforced acrylic latex composite coatings: Enhanced mechanical and anticorrosion performances via barrier and interface passivation, *Prog. Org. Coat.*, 2026, **210**, 109649, DOI: 10.1016/j.porgcoat.2025.109649.
19 T. Kouser, F. Nur, A. Aliyu, *et al.*, Applications of Epoxy Resins as a Coating Technology in Fluid Systems, *ChemBioEng Rev.*, 2025, **12**, 2, DOI: 10.1002/cben.70000.
20 Y. Tang, *et al.*, Resorcinol–formaldehyde resin combining epoxy resin as composite coating with efficient anti-corrosion resistance and anti-biofouling capacity, *Prog. Org. Coat.*, 2025, **203**, 109177, DOI: 10.1016/j.porgcoat.2025.109177.
21 X. Wang, *et al.*, Improving the performance of acrylic-epoxy ester hybrid coatings with phosphate monomers, *Polym. Chem.*, 2024, **15**, 2265–2276, DOI: 10.1039/d4py00131a.
22 M. Barshutina, *et al.*, Biomimetic Silicone Surfaces for Antibacterial Applications, *Polymers*, 2025, **17**, 213, DOI: 10.3390/polym17020213.
23 H. Chuanbo, *et al.*, Preparation of Poly(o-ethoxyaniline)-nano SiC Composite and Evaluation of Its Corrosion Resistance Properties, *J. Alloys Compd.*, 2017, **717**, 98–107, DOI: 10.1016/j.jallcom.2017.05.111.
24 J. Wang, X. Wang, X. Sun, *et al.*, Investigate the performance of functional coatings with physically modified boron nitride composite fillers, *Prog. Org. Coat.*, 2025, **205**, 109309, DOI: 10.1016/j.porgcoat.2025.109309.
25 D. Rane, *et al.*, Superwettable surfaces and factors impacting microbial adherence in microbiologically-influenced corrosion: a review, *World J. Microbiol. Biotechnol.*, 2024, **40**, 98, DOI: 10.1007/s11274-024-03886-3.
26 A. Khan, *et al.*, Surface roughness influence on extracellular electron microbiologically influenced corrosion of $C_{10\text{-}18}$ carbon steel by Desulfovibrio ferrophilus IS5 biofilm, *Bioelectrochemistry*, 2024, **159**, 108731, DOI: 10.1016/j.bioelechem.2024.108731.
27 Y. Meng, *et al.*, Preparation and Characterization of Low Surface Energy Waterborne Acrylic Anticorrosion and Antibacterial Coatings Applied in Maritime Protection, *ACS Appl. Polym. Mater.*, 2025, **7**, 1307–1317, DOI: 10.1021/acsapm.4c03002.
28 Y. Lin, *et al.*, Rapid release of high-valent silver ions from water-soluble porphyrin complexes to enhance the direct killing of Methicillin-Resistant Staphylococcus aureus, *Acta Biomater.*, 2025, **192**, 419–430, DOI: 10.1016/j.actbio.2024.12.004.
29 G. Tailor, *et al.*, Biofilm inflection via chemically synthesized silver and nickel nanoparticles, *Discover Appl. Sci.*, 2024, **7**, 30, DOI: 10.1007/s42452-024-06182-9.
30 J. S. Afolayan, *et al.*, A rapid microwave approach for 'one-pot' synthesis of antibiotic conjugated silver nanoparticles with antimicrobial activity against multi-drug resistant bacterial pathogens, *Colloids Surf., B*, 2025, **245**, 114280, DOI: 10.1016/j.colsurfb.2024.114280.
31 V. Demchenko, *et al.*, Fabrication of polylactide composites with silver nanoparticles by sputtering deposition and their antimicrobial and antiviral applications, *Polym. Int.*, 2025, **74**, 207–216, DOI: 10.1002/pi.6707.

32 G. Balbinot, *et al.*, Silver core-shells particles as antibacterial filler for adhesive resins, *Int. J. Adhes. Adhes.*, 2025, **138**, 103916, DOI: 10.1016/j.ijadhadh.2024.103916.
33 C. Li, *et al.*, Synthesis and synergistic effects of antibacterial and corrosion inhibition based on concentrated hydrosols of silver nanoparticles, *Corros. Sci.*, 2024, **233**, 112102, DOI: 10.1016/j.corsci.2024.112102.
34 T. Yang, *et al.*, Preparation and characterization of cellulose nanocrystal coated with silver nanoparticles with antimicrobial activity by enzyme method, *Int. J. Biol. Macromol.*, 2025, **292**, 139212, DOI: 10.1016/j.ijbiomac.2024.139212.
35 W. Lu, *et al.*, Serine-modified silver nanoparticle porous spray membrane: A novel approach to wound infection prevention and inflammation reduction, *Int. J. Pharm.*, 2025, **670**, 125120, DOI: 10.1016/j.ijpharm.2024.125120.
36 A. Telli, *et al.*, In-situ functionalization of cotton fabrics with polydopamine and silver nanoparticles for multifunctional applications, *Cellulose*, 2024, **32**, 1377–1391, DOI: 10.1007/s10570-024-06342-5.
37 P. S. Umoren, *et al.*, Assessment of olive leaf extract–mediated chitosan–silver nanocomposites as antibacterial and biocorrosion mitigation agents, *Cellulose*, 2024, **31**, 1705–1727, DOI: 10.1007/s10570-023-05704-9.
38 M. G. M. Zeariya, *et al.*, Improvement of antibacterial activity of AgNPs@PVA-PVP ternary nanocomposite films followed by gamma-ray irradiation treatment for biomedical applications, *Radiat. Phys. Chem.*, 2025, **226**, 112345, DOI: 10.1016/j.radphyschem.2024.112345.
39 L. Zheng, *et al.*, Fabrication of Highly Stable Polyurushiol-Decorated Silver Nanoparticles and Evaluation of Their Antibacterial and Anti-Microalgae Activities, *J. Inorg. Organomet. Polym. Mater.*, 2024, **35**, 570–582, DOI: 10.1007/s10904-024-03313-y.
40 J. Luo, *et al.*, Integration of multistructured microcapsules with self-healing and antimicrobial properties into polymer coatings for enhanced metal surface protection, *Colloids Surf., A*, 2025, **707**, 135895, DOI: 10.1016/j.colsurfa.2024.135895.
41 G. Li, *et al.*, Dual-Function Hybrid Coatings Based on Polytetrafluoroethylene and Cu_2O for Anti-Biocorrosion and Anti-Wear Applications, *Coatings*, 2024, **14**, 592, DOI: 10.3390/coatings14050592.
42 Q. Tian, *et al.*, High-solid and water-based epoxy resin anticorrosion coatings for complex construction environments: Synergistic effect of inorganic-organic hybrid and grafted long chain structure, *Appl. Surf. Sci.*, 2025, **687**, 162299, DOI: 10.1016/j.apsusc.2025.162299.
43 L. Fan, *et al.*, Design of superhydrophobic coatings fabricated by spraying for anti-icing, *J. Phys. Conf. Ser.*, 2024, **2720**, 012005, DOI: 10.1088/1742-6596/2720/1/012005.
44 L. Zhao, *et al.*, Layer-by-Layer-Assembled Antifouling Films with Surface Microtopography Inspired by Laminaria japonica, *Appl. Surf. Sci.*, 2020, **512**, 145564, DOI: 10.1016/j.apsusc.2020.145564.